

Titan: Evidence for Seasonal Change—A Comparison of *Hubble Space Telescope* and *Voyager* Images

JOHN CALDWELL,^{*,†,1} CINDY C. CUNNINGHAM,[†] DAVID ANTHONY,^{*,†} H. PETER WHITE,^{*,†} E. J. GROTH,[‡] H. HASAN,[§] K. NOLL,[§] P. H. SMITH,[¶] M. G. TOMASKO,[¶] AND H. A. WEAVER[§]

^{*}Department of Physics and Astronomy, York University, Toronto, Ontario; [†]Space Astrophysics Laboratory, Institute for Space and Terrestrial Science, Concord, Ontario; [‡]Physics Department, Princeton University, Princeton, New Jersey; [§]Space Telescope Science Institute, Baltimore, Maryland; and [¶]Lunar and Planetary Laboratory, University of Arizona, Tucson, Arizona

Received October 4, 1991; revised January 17, 1992

Images of Titan were obtained by the *Hubble Space Telescope* (*HST*) on 26 August 1990. Comparison with *Voyager* 1 and *Voyager* 2 images obtained 10 and 9 years earlier shows that the seasonal hemispheric brightness asymmetry has reversed near 440 and 550 nm wavelengths, with the northern hemisphere now being brighter. An additional, noisy *HST* image at 889 nm wavelength, for which there are no analogous *Voyager* data, suggests that the southern hemisphere may have been brighter than the northern at that wavelength in 1990. © 1992 Academic Press, Inc.

INTRODUCTION

As part of its Early Release Observation (ERO) program, the *Hubble Space Telescope* (*HST*) obtained three images of Titan during a single orbit on 26 August 1990 using PC chip 6 of the Wide Field/Planetary Camera (WFPC). The wavelengths were 439, 547, and 889 nm, respectively.

Even before the *Voyager* spacecraft produced its first spatially resolved images of Saturn's moons, Titan had been observed to be slowly changing its blue (472 nm) and yellow (551 nm) albedos by as much as 10% over a 7-year interval (Lockwood and Thompson 1979). Early speculation about the cause of this change centered on upper atmosphere chemistry driven by the 11-year periodicity in the Sun's UV output (Allen *et al.* 1980, Yung *et al.* 1984).

Voyagers 1 and 2 obtained the highest resolution images of Titan during their encounters with Saturn in 1980 and 1981, respectively (Fig. 1). One of the important results from that time was that Titan exhibited a distinct hemi-

spherical asymmetry at visual wavelengths (Smith *et al.* 1981). The *Voyager* images and several more years of ground based observations shifted the earlier interpretation of this asymmetry to a seasonal variation in the hemispheric albedo pattern (Sromovsky *et al.* 1981, Lockwood *et al.* 1986). This model predicts that the north–south asymmetry observed by *Voyager* in 1980–1981 would diminish to a uniform disk by late 1987, after which the hemispheric asymmetry would be reversed with the southern hemisphere appearing darker than the northern. Atmospheric albedo response apparently lags seasonal forcing by nearly one-quarter of a Titan year (Flasar and Conrath 1991). Searches for variations over shorter time scales, such as Titan's 16-day orbit around Saturn, have found no variations larger than 1% (Lockwood 1975).

Comparison of the *Voyager* Titan images with the *HST* 439-nm (Fig. 2) and 547-nm images therefore provides an opportunity to test the seasonal model, since more than a quarter of the Titan year has passed between the two epochs.

There is no analogous image with the *Voyager* data set for comparison to the *HST* 889-nm image. The latter is essentially independent of the *Voyager* and *HST* visual images because, by design, the filter transmits only photons within the strong methane (CH_4) band at that wavelength, and therefore samples altitudes significantly higher than the shorter wavelength images.

Variability in the infrared also exists, although much less work has been done than on the visible albedo observations discussed above. Cruikshank and Morgan (1980) detected variations in photometric observations with the *J* (1.25 μm) and *K* (2.2 μm) filters over a period of more than 2 months. The data suggest a possible 32-day period, although this has never been independently verified. Recently, Noll and Knacke (1991) have reported observations using the *M* filter (4.8 μm) that show a decrease in

¹ To whom reprint requests should be addressed at Space Astrophysics Laboratory, Institute for Space and Terrestrial Science, 2700 Steeles Ave. W., Concord, Canada, ON L4K 3C8.

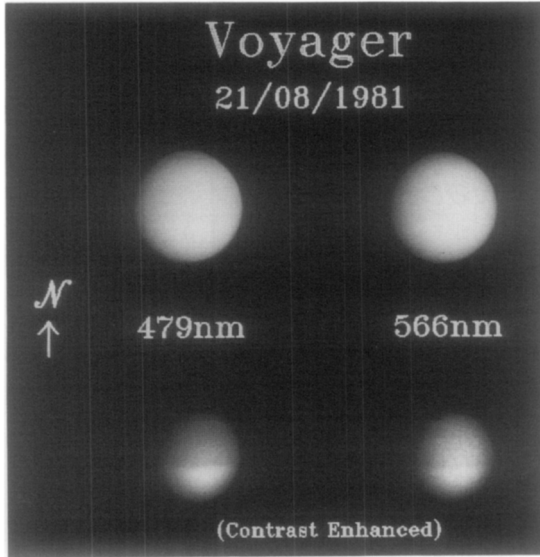


FIG. 1. *Voyager 2* images of Titan, selected to match the *HST* images as closely as possible with respect to wavelength, pixel size, and observing geometry (see Table I). The largest discrepancy is in subtelescope and subsolar latitude. The lower two images are identical to the upper two except they have been contrast enhanced by uniformly raising each pixel to the fifth-power.

Titan's albedo by more than a factor of two compared to the only other published observations at this wavelength, which were made in the winter of 1973–1974. The long gap between observations precludes a firm identification of periodicity in the 4.8- μm variations, but an atmospheric seasonal model could be eliminated. Titan was at nearly

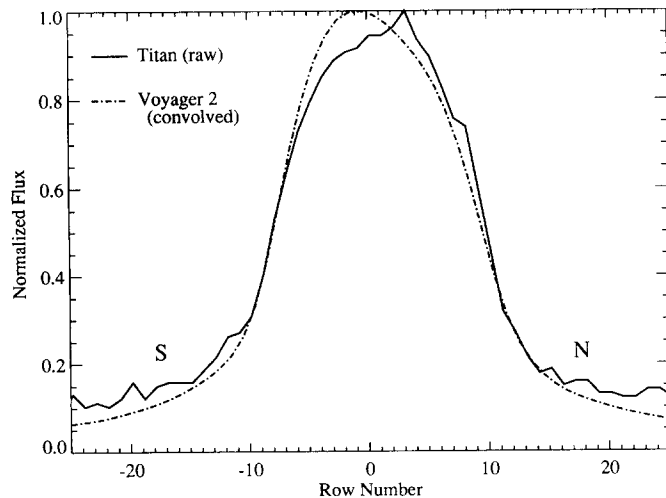


FIG. 2. North-to-south cuts through the raw 439-nm *HST* data and through the 479-nm *Voyager* data, where the latter have been convolved with the *HST* PSF, to produce comparable data. The different seasonal asymmetries are clearly evident. The cut through the *HST* data is not affected by the notch evident in Fig. 3.

the same seasonal phase (just after solstice) for both sets of observations, so the change could not be attributed to seasonal forcing. Searches for variability at longer (IR) wavelengths have been conducted (Low and Rieke 1974) but no change was detected over 10 years of observation.

Finally, Muhleman *et al.* (1990) report radar detection of Titan using the VLA on three nights in June 1989. Statistically significant variations seem to have occurred, with the radar cross section on the middle night of the three being a factor of two higher than either the first or the third night. This result requires confirmation, but could indicate the presence of compositional variations with longitude on Titan's surface.

The different types of variability most likely occur because the respective wavelengths do not probe the same levels of the atmosphere. Radiation longward of 8 μm is sensitive to thermal structure of the stratosphere. Near-IR and mid-IR wavelengths outside strong CH_4 absorption bands probe at least as deep as the tropopause and may reach the surface (Griffith *et al.* 1991). Visible wavelength light is most sensitive to submicrometer-size aerosol particulate distributions above the tropopause. Therefore there is no a priori reason to expect that temporal trends in one wavelength band should follow changes at other wavelengths. However, this complex behavior underlines the need for observations at an array of wavelengths with a mix of instruments if progress in understanding the complex nature of Titan is to be made.

OBSERVATIONS AND REDUCTIONS

The *HST* images were obtained without planetary tracking, so that their exposure times were deliberately short, to minimize blurring due to target motion. The exposure times were: 2 sec at 439 nm, 1 sec at 547 nm, and 14 sec at 889 nm. The images all have much less than optimum exposure. In one case, 439 nm, the image is marred by a severe blemish on the chip, requiring extensive reconstruction.

The *HST* PC has a pixel size of 0.0427 arcsec, so one expects a Titan image diameter of about 20 pixels in this camera. Visual inspection of the images reveals that this is the case, but the images are strongly influenced by the well known spherical aberration problem with the telescope primary optics. Deconvolution is therefore critical in extracting the maximum information from the images.

Observing parameters for both the *HST* and *Voyager* images studied are summarized in Table I.

Each of the three *HST* Titan images had numerous pixels which were anomalously exposed by cosmic rays. However, the percentage of such anomalous events compared to the total image was very low and they were easily identifiable. Thus, the effect could be completely

TABLE I
Observing Parameters for Titan Images

	<i>HST</i>			<i>Voyager 2</i>	
	Blue	Green	Near IR	Blue	Green
Wavelength (nm)	439	547	889	479	566
Exposure time (sec)	2.0	1.0	14.0	1.92	1.92
\sqrt{N} : Signal to noise ratio at center of Titan image	28	45	17		
Date	Aug. 26, 1990			Aug. 12, 1981	Aug. 16, 1981
Phase angle		4.0°		3.7°	3.5°
Subtelescope Latitude		24.0°		11.2°	9.9°
Subsolar Latitude		23.0°		7.9°	7.9°
	Saturnian northern summer solstice			Saturnian vernal equinox	
	Dec. 11, 1987			Mar. 3, 1980	

corrected. A bias level was also subtracted from each frame. In the case of the 547- and 889-nm images, a flat-field correction was also applied. Two separate deconvolution techniques, the Lucy iteration method (Lucy 1974) and the Fourier inverse-quotient method (Brault and White 1971), were then applied to each of these images.

Extensive image reconstruction was necessary in the case of the Titan image at 439 nm. The Titan disk fell on a part of the WF/PC CCD chip number 6 that has a blemish. The blemish is due to the shadow of a dust particle in the optical path. Astronomical images are not illuminated the same way as diffuse flat fields because of spherical abberation. The blemish therefore cannot be corrected with flat-fielding. The result was that there was a rather large "notch" in the Titan disk at the east equatorial limb (see Fig. 3).

Attempts at deconvolving the 439-nm Titan image without repairing the blemish were unsatisfactory. This is because no real distribution of incident light, without erroneous shadowing, could produce the raw data as observed. Several different techniques for reconstructing this portion of the Titan disk were therefore explored. The technique which gave the best result to replace the bad pixels by their counterparts from the opposite limb of Titan. Deconvolution of this reconstructed image was then performed.

A point spread function (PSF) is a representation of how light from a point source would be imaged by a given known optical system. In the absence of contemporaneously observed PSFs for these data, theoretical PSFs were calculated as a function of wavelength, location on the CCD, and telescope focus by H. Hasan. The PSFs contain all known optical path features in the *HST*. The results presented below show that these PSFs were adequate for the analysis presented here.

FOURIER DECONVOLUTION

The Fourier deconvolution technique involves transforming the Titan image, $s(x)$, and its corresponding normalized PSF, $r(x)$ into Fourier space and then dividing the Fourier transform of the Titan image, $S(f)$, by the Fourier transform of the PSF, $R(f)$. The result is then convolved with the Fourier transform of a Gaussian, $G(f)$, which has a FWHM about equal to that of the core of the PSF. The last step acts to restore the telescope response that would have been present without spherical abberation.

$$U(f) = \frac{S(f)}{R(f)}, \quad (1)$$

where $U(f)$, $S(f)$, and $R(f)$ are the Fourier transforms of the "true" Titan image, the raw Titan image, and the PSF, respectively. The "true" image, $u(x)$, can now be recovered by

$$u(x) = \mathcal{F}^{-1}[U(f) \cdot G(f)] \quad (2)$$

where \mathcal{F}^{-1} denotes the inverse Fourier transform.

This technique works best for high signal-to-noise (S/N) images because noise is amplified strongly (Brault and White 1971). When the image has low S/N, as is the case for these Titan images, it is very difficult to separate the signal from the noise. Both are given equal weighting by this technique.

A regular characteristic of the Fourier-deconvolved Titan images is that the Titan disk is surrounded by a narrow dark ring and by a broader bright ring. This "ringing" effect is seen in all three deconvolved Titan images to varying degrees. Examples of the magnitudes of these "side lobe" features are shown in Figs. 4a, 4b, and 5 for the 439, 547, and 889 nm Titan images, respectively.

LUCY DECONVOLUTION

The Lucy iterative method of image deconvolution (Lucy 1974) was also performed on the Titan images. The advantage of this nonlinear technique is the fact that the flux distribution remains positive. Also the enhancement of high frequency noise features is not as pronounced as in fourier inversion. Drawbacks of the method include the relatively large amount of computer time required and the lack of a simple numerical criterion for stopping the iterations.

The first iteration to each of the image deconvolutions was arbitrarily set to a flat distribution, where the total integrated flux of the flat was equal to that of the raw data. A χ^2 comparison of the raw image is made to each iteration of the restored image convolved with the PSF. In principle, one could iterate many times, until the χ^2 fit to the

data is minimized. However, our findings indicate that for low S/N images, the minimum χ^2 is reached very slowly and the improvement in the resulting image does not continue indefinitely as the iterations continue.

This is consistent with initial tests of the method by Lucy (1974), which included a χ^2 check of a deconvolved distribution with the known distribution of some test data (Lucy 1974, his Fig. 2). He explicitly showed that it was possible to achieve a worse fit to the true data by continuing the iterations too far.

The major problem with the Lucy method is therefore to know when to stop iterating. The stopping criterion in this paper is derived from two pseudo- χ^2 parameters that are similar to the ones outlined in the original paper (Lucy 1974). Using his notation, we form

$$\chi^2(\phi^r) = \sum_{k=1}^N \frac{(\phi_k^r - \tilde{\phi}_k^r)^2}{\phi_k^r} \Big| (N-1), \quad (3)$$

$$\chi^2(\psi^r) = \sum_{k=1}^N \frac{(\psi_k^r - \tilde{\psi}_k^r)^2}{\psi_k^r} \Big| (N-1), \quad (4)$$

where $\tilde{\phi}$ is the “raw” data, ψ^r is the r th iteration of the approximation to the data, and ϕ^r is the r th approximation convolved with the point spread function. When $\chi^2(\psi^r) > \chi^2(\phi^r)$, we terminate the iterations.

After each step of the iteration, we compare the raw data with both the restored image and the restored image convolved with the PSF. The second comparison indicates how well the restored image, blurred with the PSF, matches the data. If we have recovered the “true” image during deconvolution, then blurring it would reproduce the raw image exactly. Of course, pixel-to-pixel noise, sky background noise, and inexact PSFs will limit this recovery. In general, this comparison will improve from one iteration to the next, but successive improvements soon become very small.

The first comparison, of the restored image with the raw image, indicates the improvement over the original data. Because the initial approximation is a flat, this difference is initially large and decreases with each iteration until a point where the restored image is at least as good as the raw image in approximating the true image. The χ^2 function is at a minimum at this iteration. Obviously, iterations could proceed beyond this point to restore the data to a state that is statistically closer to the truth than the original data itself. However, χ^2 residuals increase. This is because the true distribution is being matched more closely and thus there is a divergence between the restored and the raw data.

If interpreted in this manner, subsequent iterations indicate that the approximation to the true image continues to improve. However, we have adopted a very conservative

stopping criterion. The iteration when the two χ^2 residuals are equal is the point where we stop the restoration and present our results. We are guided in the decision to adopt this conservative position by the realization that if we continued the iterations only a small number of times, the resulting Titan images would be impossible to fit with any reasonable atmospheric model. We believe that the simultaneous and apparently contradictory trends toward formal improvement of the deconvolutions and obviously nonphysical results is due to the amplification of noise in the numerical details. The formal results would imply more information than the original data actually contain. By stopping where we do, we ensure that we avoid this trap.

This criterion leads to the following stopping points: 439 nm, six iterations; 547 nm, five iterations; 889 nm, six iterations.

RESULTS

Visual inspection of the raw *HST* data, corrected for cosmic rays and bias, and flat-fielded, but not deconvolved, shows that they are not symmetric. As a first step, we convolved the *Voyager* 479-nm image with the *HST* PSF, to simulate what an *HST* image would have been like in 1981. The convolution process is completely straightforward, and is limited in accuracy only by the PSF.

A north-to-south cut through the raw *HST* 439-nm image and the corresponding cut through the convolved *Voyager* image are shown in Fig. 2. In that figure, it is immediately apparent that the seasonal asymmetry observed by *Voyager* in 1981 had changed in sense from a bright south to a bright north in 1990. It must be emphasized that the central cut through the *HST* data is completely unaffected by the notch evident in Fig. 3. This increases our confidence that the following discussion of deconvolution of the “corrected” *HST* 439-nm image shown at the left of Fig. 3 is valid. Our correction is not responsible for introducing the basic north–south asymmetry in the *HST* 439-nm image.

Figures 4a, 4b, and 5, respectively, show the results of deconvolving the three *HST* images. In Figs. 4a and 4b, north-to-south cuts through the centers of 439- and 547-nm images deconvolved by both techniques are compared with similar cuts through the *Voyager* 479- and 566-nm images. In each of these images, differences may be seen between the two deconvolution techniques. The ring around Titan produced by the Fourier deconvolution may be seen in cross-section at both wavelengths, approximately 10 pixels outside the limb.

It is also apparent that the disk of Titan in each Lucy deconvolution is narrower than the corresponding disk in the Fourier deconvolution, although the remaining wings

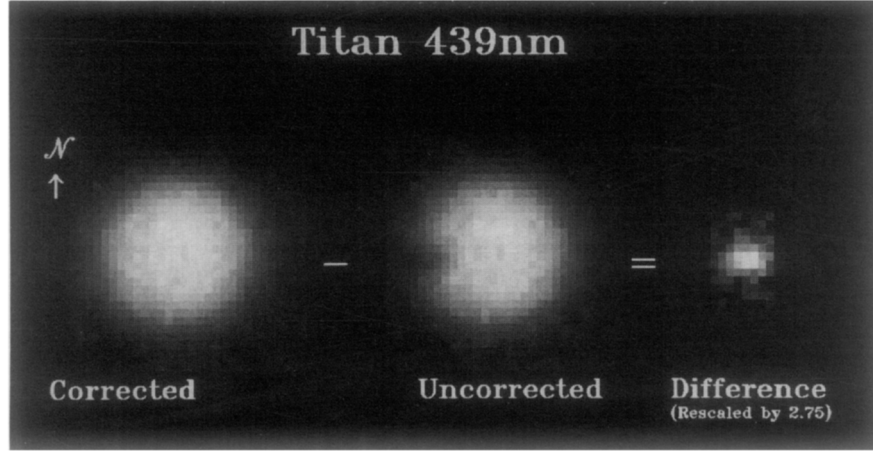


FIG. 3. An image reconstruction was necessary to correct for an interfering blemish caused by dust in the optical path. The best technique involved replacing the pixels in the blemish with their counterparts from Titan's other limb.

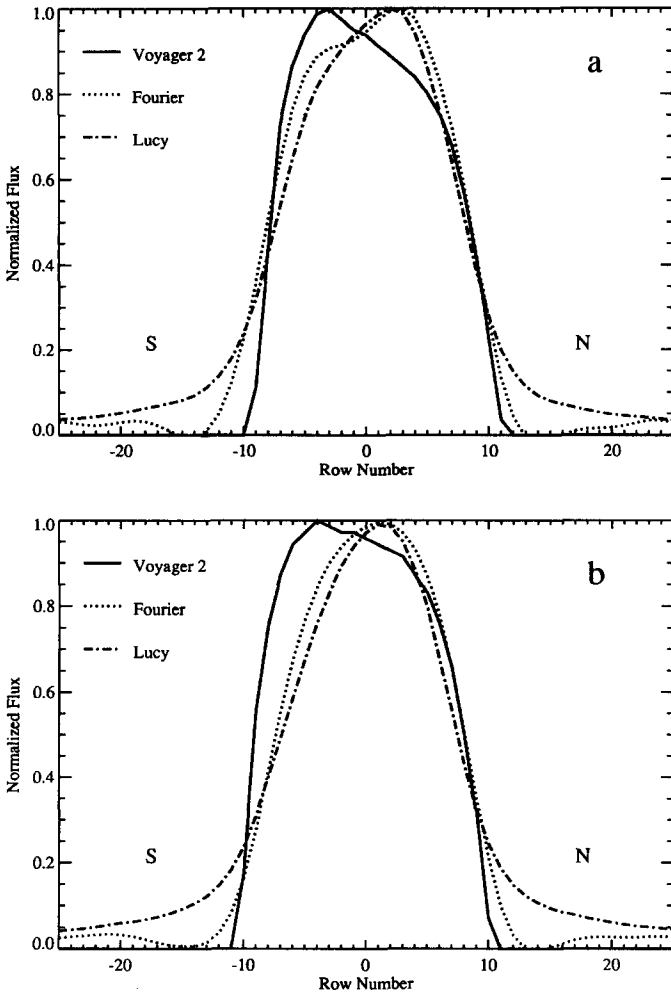


FIG. 4. (a) North-to-south cuts through images at 439 nm (*HST*, deconvolved) and 479 nm (*Voyager*), showing reversed hemispheric seasonal asymmetries. (b) Similar to (4a) except at 547 nm and 566 nm.

in the Lucy version are greater. By increasing the number of iterations in the Lucy process, it would be possible to decrease the flux in the wings, while producing an ever more narrow disk. As stated in the previous section, we have decided not to do so, and believe that our stopping points for the iterative procedure are the best ones for the data we have.

The change in the sense of the north–south asymmetry on Titan is clearly seen at both wavelengths, with the magnitude of the asymmetry being greater at the shorter wavelength.

Figure 5 shows the raw *HST* 889-nm image compared with both Lucy and Fourier deconvolutions. The data in this image are extremely noisy. The low signal-to-noise ratio in this image causes the results of the deconvolutions

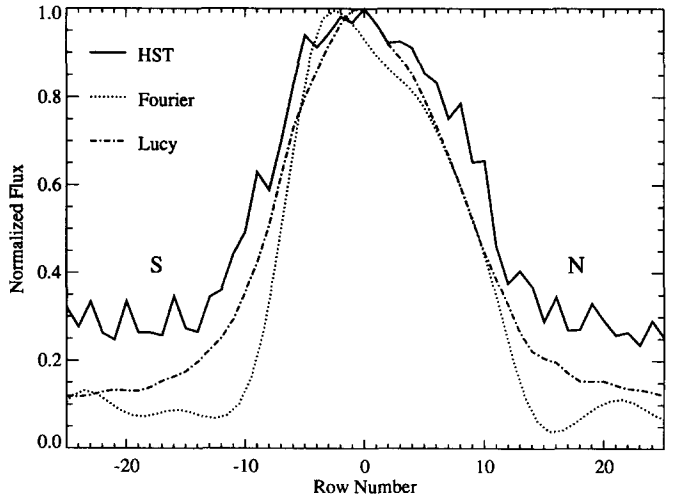


FIG. 5. North-to-south cuts through the *HST* image at 889 nm for the raw data and for both deconvolution techniques.

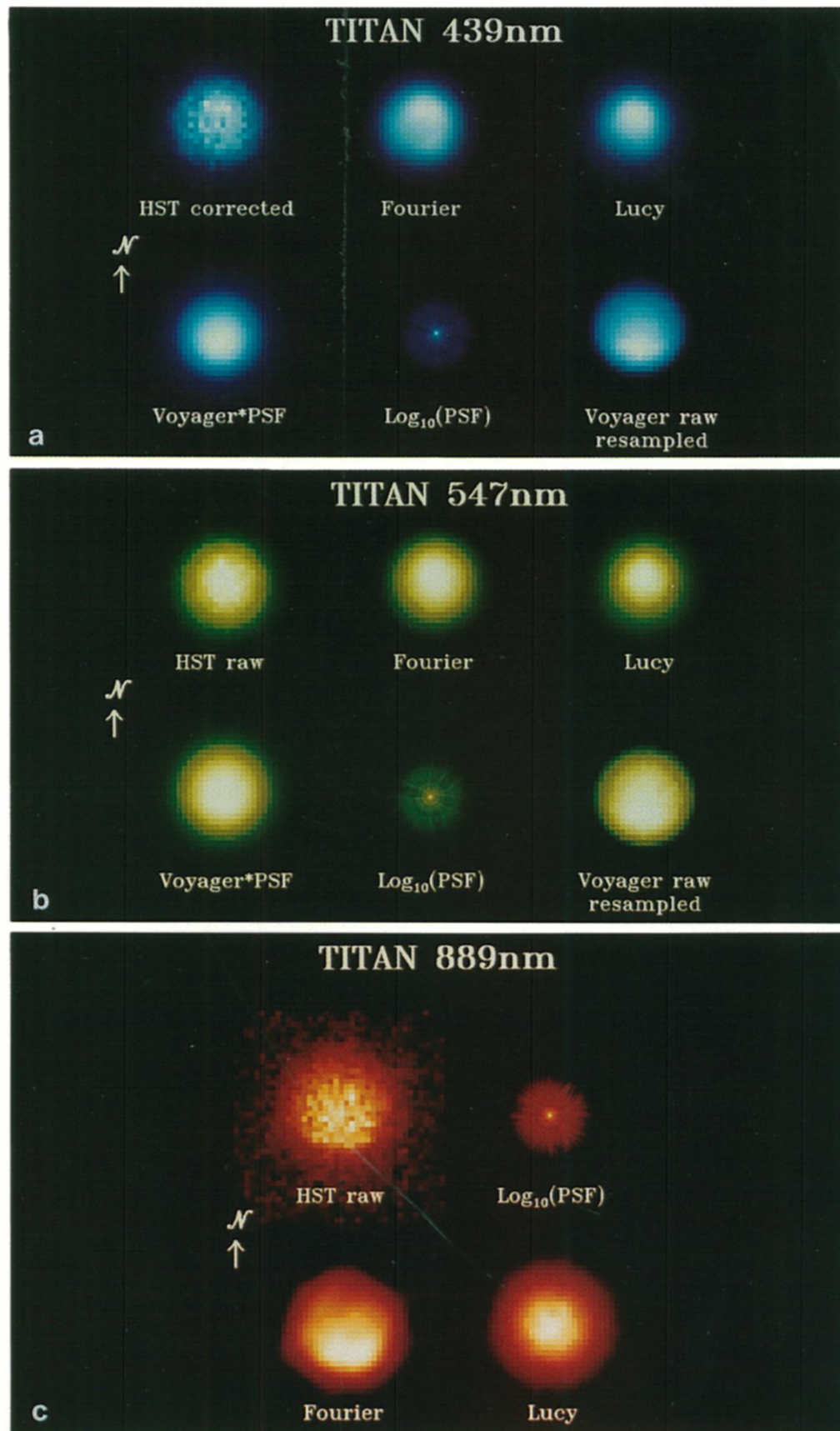


TABLE II
Model Parameters for Titan Images

	<i>HST</i>		Voyager 2	
	Blue	Green	Blue	Green
Radius in pixels	10.3	10.3	10.3	10.3
Subtelescope latitude	24.0°	24.0°	11.2°	9.9°
Latitude of asymmetry	34.0°	30.0°	-7.0°	-2.0°
Northern <i>B</i>	1.00	1.00	0.86	0.91
Northern <i>x</i>	0.60	0.60	0.45	0.40
Southern <i>B</i>	0.88	0.92	1.00	1.00
Southern <i>x</i>	0.60	0.70	0.55	0.40

to be less certain. However, it is clear that in both the raw and the deconvolved versions, there is a difference between this figure and Figs. 4a and 4b. The raw data and the Fourier deconvolution both strongly indicate that the southern hemisphere appears brighter at this wavelength than the northern. The Lucy deconvolution is more suggestive of a symmetric brightness distribution. The difference between the two deconvolution techniques is undoubtedly due to the high noise level of this figure. In any case, there is no suggestion at this wavelength that the northern hemisphere could be brighter, which is contrary to the case at shorter wavelengths.

There are no *Voyager* data at or near this wavelength with which to compare and no models were generated. The qualitative difference between Fig. 5 and Figs. 4a and 4b is certainly because the 889-nm image contains only photons reflected in the very strong methane absorption band at this wavelength, and therefore, by design, it samples only very high altitudes on Titan.

Figures 6a, 6b, and 6c show the Titan *HST* images at all three wavelengths, both as raw data and deconvolved by both techniques. Also included are the PSFs, and for the two visual wavelength images, their *Voyager* counterparts.

Simple models have been created for comparison between the *HST* 439- and 547-nm images, and their *Voyager* 2 counterparts. The model parameters included: (1) Titan's optical radius, (2) a single latitude, not restricted to be the equator, which divides Titan into two parts, each with different brightness characteristics, and (3) the brightness characteristics of the northern and southern parts. The purpose of the models ultimately is to demon-

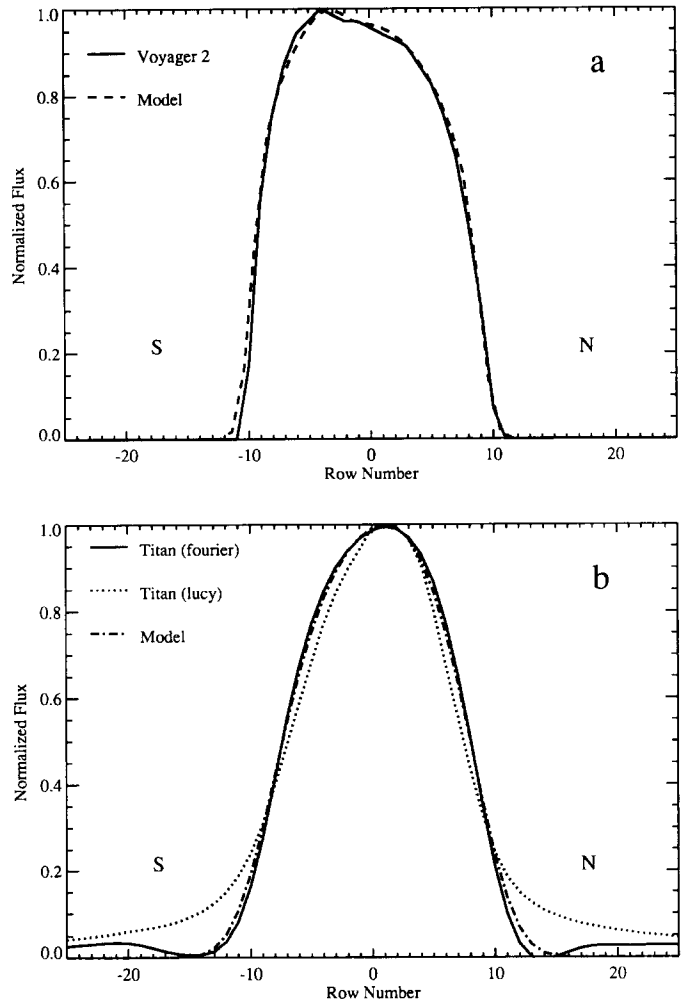


FIG. 7. (a) A model, using the parameters from Table II, convolved with a 2-pixel Gaussian, compared to the *Voyager* green (566 nm) image from which the model was derived. (b) Similar to (a) but with the model convolved with a 4-pixel Gaussian and compared to the *HST* green (547 nm) image from which the model was derived.

FIG. 6. (a) The Titan 439-nm image, including correction, plus Fourier and Lucy deconvolutions, with a *Voyager* 479-nm image (resampled to *HST* pixel size). Also shown is the log of the *HST* PSF at this wavelength. It is exhibited on a log intensity scale so that detail in the wings of the PSF can be seen. The result of convolving the *Voyager* image with the *HST* PSF, for comparison to the *HST* image (Fig. 3) is also given. (b) Same as (a), except at 547 nm. However, the *HST* data at this wavelength do not require correction for blemishes before deconvolution. (c) similar to (a) and (b), except at 889 nm. There are no *Voyager* images for comparison.

strate the difference between the actual *HST* observations and the appearance Titan would have had in 1990 if its reflectivity had not changed since 1980.

No attempt has been made to increase the complexity of the model beyond this. In particular, there is no analog of the northern "polar hood" seen in some of the higher resolution *Voyager* images (Smith *et al.* 1981). This exclusion is not important because the *Voyager* feature would

fill only one *HST* pixel. Furthermore, the northern hemisphere has clearly changed since the *Voyager* observations, so there is no compelling reason to believe the feature still exists. If an analogous feature has developed at the now darker southern pole, we could not see it because that pole is now tilted away from the *HST*.

The *Voyager 2* images were chosen such that image conditions, such as pixel resolution, subsatellite latitude, and phase angle (J. Swann, private communication, 1991), were as similar to the *HST* images as possible (see Table I). In both cases, the *Voyager 2* images were demagnified by a factor of 5.9 to match their *HST* counterparts.

We used the same Titan radius as Courtin *et al.* (1990): 2935 km, which corresponds to 0.438 arcsec (or 10.3 PC pixels) at the distance of Titan, 9.245 AU. This corresponds very well with the visually inspected radius of approximately 10 pixels for the two images, and was used in the modeling. The original *Voyager* images had radii of approximately 50 *Voyager* pixels, thus their spatial resolution was on the order of 20–25 times higher than the *HST* images.

Within each of the two regions to which we restrict our model, the brightness is determined by a normal reflectivity (B) and a cosine power law, with exponent x . The best values for these parameters, determined by visual comparison of north-to-south and east-to-west cuts through *Voyager* and *HST* images with approximately convolved models, are included in Table II.

$$B = B_0 \cos^x \Theta, \quad (5)$$

where B_0 is the brightness level assigned to the hemisphere as outlined in Table II and Θ is the latitude.

Figure 7a compares *Voyager* 566-nm north-to-south cuts with the best-fitting model, the latter being convolved with a FWHM 2-pixel Gaussian. Figure 7b compares *HST* 547 nm north-to-south cuts with best-fitting models, the latter being convolved with a FWHM four-pixel Gaussian, which is equivalent to the smoothing done in the last step of the Fourier deconvolution procedure. These comparisons were also done with the *Voyager* 479-nm and *HST* 439-nm images, showing a similar brightness asymmetry change as demonstrated by the above two figures.

Using the *Voyager* parameters thus determined, we have replotted in Fig. 8a the unconvolved *Voyager* green model, adjusted to the *HST* observing conditions (subtelescope latitude = 24° instead of 10°) together with the corresponding, unconvolved *HST* model at the present geometry. This figure represents our estimate of the quantitative difference in the green appearance of Titan between northern early spring and midsummer seasons, that is, 1981 and 1990. Figure 8b similarly represents the quantitative change in the blue appearance of Titan between seasons.

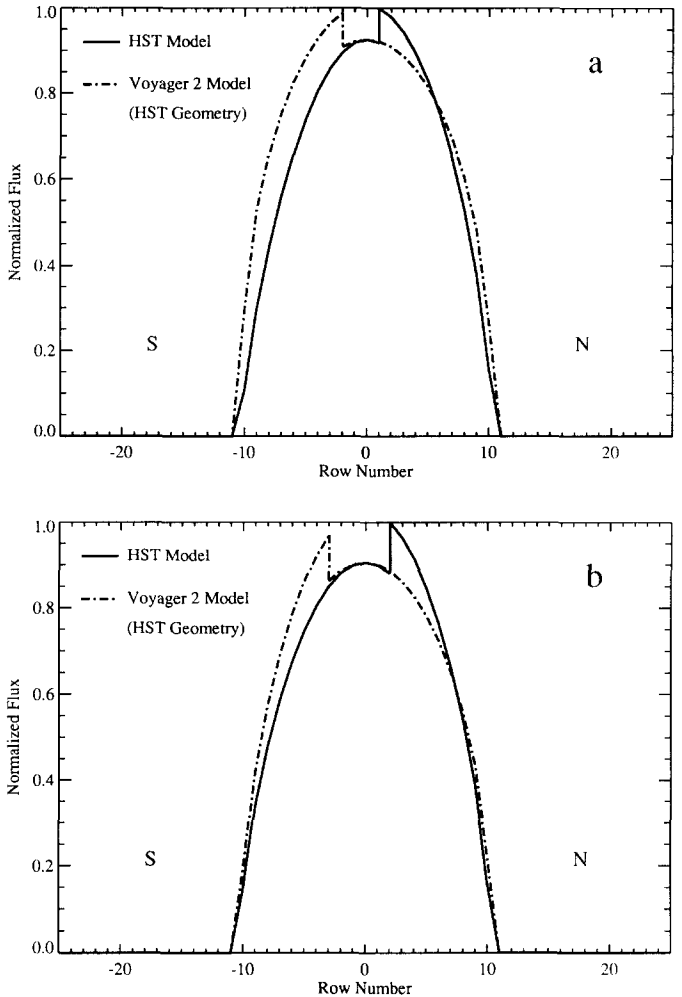


FIG. 8. (a) The nonconvolved *HT* green model from Table II compared to the nonconvolved *Voyager* green model from Table II, where the latter has been adjusted to the same observing geometry as the former, that is, subtelescope latitude = 24°. The *Voyager* model shows how Titan would have appeared in *HST* images, if the atmospheric structure observed in 1981 had remained constant in time. (b) Same as (a) except at 439 nm (*HST*) and 479 nm (*Voyager 2*).

CONCLUSIONS

Titan's albedo pattern, as shown by the *HST* images reported in this paper, is adequately explained by a seasonal model. At visual wavelengths, Titan's northern hemisphere is ~10% brighter than the southern one, in contrast to its appearance during the *Voyager* encounter a decade ago. In several respects the images are not optimal: the exposure times were too short, planetary motion was not tracked, and a chip blemish marred the blue image. Therefore, additional observations with *HST* are desirable, both to improve upon the quality of the present data and to monitor the continuing seasonal change on Titan.

ACKNOWLEDGMENTS

Based on observations with the NASA/ESA *Hubble Space Telescope*, obtained at the Space Telescope Science Institute, which is operated by the Association of Universities for Research in Astronomy, Inc., under NASA Contract NAS5-26555. We thank J. Swann of the United States Geological Survey in Flagstaff, Arizona for expert assistance in deriving the observational geometry for the Titan images discussed above. This research is supported by NASA Grant NAS5-30294 at York University.

REFERENCES

- ALLEN, M., J. P. PINTO, AND Y. L. YUNG 1980. Titan: Aerosol photochemistry and variations related to sunspot cycle. *Astrophys. J.* **242**, L125–L128.
- BRAULT, J. W., AND O. R. WHITE 1971. The analysis and restoration of astronomical data via the fast Fourier transform. *Astron. Astrophys.* **13**, 169–189.
- COURTIN, R. R. WAGENER, C. P. MCKAY, J. CALDWELL, K.-H. FRICKE, P. RAULIN, AND P. BRUSTON 1990. UV Spectroscopy of Titan's Atmosphere, Planetary Organic Chemistry and Prebiological Synthesis: II. Interpretation of New IUE Observations in the 220–335 nm Range. *Icarus*, **90**, 43–56.
- CRUIKSHANK, D. P., AND J. S. MORGAN 1980. Titan: Suspected near-infrared variability. *Astrophys. J.* **235**, L53–L54.
- FLASAR, F. M., AND B. J. CONRATH 1991. Titan's stratospheric temperatures: A case for dynamical inertia? *Nature* **292**, 693–698.
- GRIFFITH, C. A., T. OWEN, AND R., WAGENER 1991. Titan's surface and troposphere, investigated with groundbased, near-infrared observations. *Icarus*, **93**, 362–378.
- LOCKWOOD, G. W. 1975. The secular and orbital brightness variations of Titan. *Astrophys. J.* **195**, L137–L139.
- LOCKWOOD, G. W., D. T. THOMPSON 1979. A relationship between solar activity and planetary albedos. *Nature* **280**, 43–45.
- LOCKWOOD, G. W., B. L. LUTZ, D. T. THOMPSON, AND E. S. BUS 1986. The albedo of Titan. *Astrophys. J.* **303**, 511–520.
- LOW, F. J., AND G. H. RIEKE 1974. Infrared photometry of Titan. *Astrophys. J.* **190**, L143–L145.
- LUCY, L. B. 1974. An iterative technique for the rectification of observed distributions. *Astrophys. J.* **79**, 745.
- MUHLEMAN, D. O., A. W. GROSSMAN, B. J. BUTLER, M. A. SLADE 1990. Radar reflectivity of Titan. *Science*, **248**, 975–980.
- NOLL, K. S., AND R. F. KNACKE 1992. Titan fades at 5 μm : Photometric and spectrophotometric evidence. Submitted for publication.
- SMITH, B. A. *et al.* 1981. Encounter with Saturn: *Voyager 1* imaging science results. *Science* **212**, 163.
- SMITH, B. A. *et al.* 1989. Voyager 2 at Neptune: Imaging science results. *Science* **246**, 1422–1449.
- SROMOVSKY, L. A., V. E. SUOMI, J. B. POLLACK, R. J. KRAUSS, S. S. LIMAYE, T. OWEN, H. E. REVERCOMB, AND C. SAGAN 1981. Implications of Titan's north–south brightness asymmetry. *Nature* **292**, 698–702.
- YUNG, Y. L., M. ALLEN, AND J. P. PINTO 1984. Photochemistry of the atmosphere of Titan: Comparison between model and observations. *Astrophys. J. Suppl.* **55**, 465–506.